1 **Optogenetic activation of nonhuman primate cortical and subcortical brain circuits highlights**

2 **detection capabilities of MEG source imaging**

3

4 Alberto, GE[1*†]; Stapleton-Kotloski, JR[2,4†]; Klorig, DC[1]; Rogers, ER[1]; Constantinidis[1], C; Daunais[3], JB;

5 Godwin, DW[1,2,3,4]

6   1.   Wake Forest School of Medicine Department of Neurobiology and Anatomy

7   2.   Wake Forest School of Medicine Department of Neurology

8   3.   Wake Forest School of Medicine Department of Physiology and Pharmacology

9   4.   Research and Education Department, W.G. (Bill) Hefner Veterans Affairs Medical Center

10   *Corresponding author

11   †These authors contributed equally.

12

13 **ABSTRACT**

14 Magnetoencephalography (MEG) measures neuromagnetic activity with high temporal, and

15 theoretically, high spatial resolution. However, the ability of magnetic source imaging (MSI) to localize

16 deep sources is uncertain. We developed an experimental platform combining MEG-compatible

17 optogenetic techniques in non-human primates (NHPs) to test the ability of MEG/MSI to image deep

18 signals. We demonstrate localization of optogenetically-evoked signals to known sources in the

19 superficial arcuate sulcus of cortex and in CA3 of hippocampus at a resolution of 750 μm^3. In response to

20 stimulation of arcuate sulcus and hippocampus, we detected activation in subcortical and thalamic

21 structures, or extended temporal networks, respectively. This is the first demonstration of accurate

22 localization of deep sources within an intact brain using a novel combination of optogenetics with

23 MEG/MSI. This approach is suitable for exploring causal relationships between discrete brain regions

24 through precise optogenetic control and simultaneous whole brain recording.

25

26 **INTRODUCTION**

27   A fundamental goal of neuroimaging is to observe and quantify brain activity across the spatial and

28   temporal resolutions at which it occurs. MEG holds particular promise for improving upon current

29   neuroimaging methods because it has identical temporal resolution to EEG, with the potential for

30   superior spatial resolution[1,2]. MEG detects biomagnetic fluctuations that co-occur with neuronal activity.

31   Unlike electric fields, biomagnetic signals are not distorted by the intervening tissues of the head prior

32   to arriving at the sensor thereby providing the estimation of the source of these signals with magnetic

33   source imaging (MSI) an inherent advantage over source localization with EEG[2]. While MEG has been

34   employed clinically for use in the pre-surgical evaluation of epilepsy[7–10] and in studies of deep structures

35   such as hippocampus[11] and amygdala[12], a detailed investigation of the resolution capabilities of MEG is

36   currently lacking.

37

38   Early studies employing simultaneous intracranial EEG and MEG in patients with epilepsy suggested that

39   MEG was unable to detect activity originating in deep structures such as the hippocampus[13–15]. Possible

40   explanations for this failure included concerns that the curved architecture of the hippocampus caused

41   magnetic fields to cancel or that the distance from the MEG sensors to hippocampus may be too great[16].

42   Theoretically however, the combination of a larger number of axial gradiometers (shown to have a

43   superior depth profile in comparison to planar gradiometers[4,16]), a low noise floor, minimal motion[5,6],

44   and appropriate use of beamformers[3,8,11] should optimize the signal-to-noise ratio (SNR) of biomagnetic

45   signals to allow sub-mm^3 localization of activity[5] throughout the volume of the brain. However, without

46   unequivocal demonstration in an *in vivo* preparation the degree to which the theoretical capabilities of

47   MSI are reflected in practice remains uncertain.

48

49   We have developed a MEG-compatible optogenetic preparation in vervet monkeys that allows

50   simultaneous optical stimulation and MEG recordings, along with associated local field potential (LFP)

51   recordings from deep and superficial structures. Stimulation and LFP recordings were achieved with an

52   optrode, which is a combined optical fiber/recording electrode[20, 50]. Optogenetic techniques are well

53   suited for use with MEG/MSI in that they are magnetically silent and allow for precise control over

54   neural population potentials through the use and activation of virally-expressed, light sensitive ion

55   channels[17]. In this report we have relied on synthetic aperture magnetometry (SAM)[3], a linearly-

56   constrained minimum variance (LCMV) beamformer method[3,8,11] with a theoretical sub-mm^3 spatial

57   resolution[4–6]. We have used SAM to convert MEG signals into whole-brain statistical parametric maps

58   (SPMs), differentiating it from more traditional EEG and MEG dipole analyses[3]. Using this combination of

59   approaches, we elicited and measured both biomagnetic and electrophysiological activity in two

60   representative brain areas, the arcuate sulcus of the cerebral cortex and within the CA3 region of the

61   hippocampus in vervet monkeys. We demonstrate the ability to selectively stimulate and detect

62   neuronal activity in these areas, as well as to accurately localize discrete optogenetically-elicited sources

63   of activity in brain regions downstream from stimulated areas. We further demonstrate the utility of

64   combining optogenetics and MEG/MSI in experimenter-controlled functional brain mapping across a

65   wide range of spatiotemporal scales. We propose that the tight temporal and spatial control over neural

66   populations afforded with optogenetics coupled with whole brain, high spatiotemporal resolution MEG

67   recordings will enable a new approach to functional neuroimaging.

68

69   **RESULTS**

70   ***Electrophysiology of Early Expression***

71   Three vervet monkeys were injected with AAV10-CaMKIIa-ChR2-eYFP and an optrode was implanted at

72   the site of transfection. After the animals had recovered, it was determined whether there was a

73   detectable LFP via the indwelling optrode during the early expression period. All reported

74   experimentation and data acquisition occurred under anesthesia. Optical pulses were delivered through

75   the implanted fiber at both the cortical and hippocampal sites to test the response of newly transfected

76   tissue to stimulation. Functional expression was determined using optogenetic intensity-response

77   curves at each site 2, 5, and 7 weeks post-injection. An optogenetically evoked potential was detectable

78   from depth recordings by 5 weeks post-expression and had stabilized by ~7 weeks (Figure 1c-e; cortical:

79   baseline (2 week) 95% confidence interval (CI) [-0.151, 0.374], post-expression (5 week) 95% CI [0.522,

80   1.12], post-expression (7 week) 95% CI [0.683, 1.09], hippocampal: baseline (2 week) 95% CI [-4.55e-3,

81   0.455], post-expression (5 week) 95% CI [1.31, 1.65], post-expression (7 week) 95% CI [1.50, 1.89]).

82

83   *MEG Recordings of Early Expression*

84   We analyzed post-surgical (2 week) MEG data using SAM. Consistent with the electrophysiological

85   recordings obtained in the same week, there were no detectable changes (local maxima or minima) in

86   the SAM statistical parametric maps (SPMs) at the site of stimulation, and the maps were qualitatively

87   similar to the pre-surgical control scans (Not shown - see Methods for beamforming parameters). We

88   conclude that expression of ChR2 at two weeks post-injection was insufficient to generate an optically

89   evoked response that could be identified using SAM, further evidence that our preparation is insensitive

90   to light stimulation in the absence of ChR2.

91

92   Post-mortem, fluorescence confocal microscopy revealed ChR2-eYFP at the targeted sites of

93   transfection, indicating uptake of the vector by the surrounding neurons and expression of the

94   transgene. Labeled neurons were observed in the posterior wall of arcuate cortex corresponding to area

95   8a of the monkey cortex[23,24] (Figure 1ai). Hippocampal imaging revealed ChR2-eYFP labeled neurons in

96   anterior dorsal hippocampus corresponding to area CA3[24] with labeled efferent connections observable

97   in the surrounding tissue (Figure 1bi). Structural MRI prior to necropsy confirmed placement of the

98   optrode in both the posterior wall of arcuate sulcus and in anterior dorsal hippocampus[25] (Figures 1aii-iii

99   and Figures 1bii-iii).

100

101   As a positive control for MSI detection and localization accuracy, we presented 119, 50 ms pulses of

102   white light to the left lower quadrant of the visual field of the left eye. (The right eye was closed.) In

103   contrast to the lack of optogenetic biomagnetic responses at 2 weeks, visual stimulation experiments

104   conducted at this time point demonstrated SAM peak voxels in the right occipital lobe (±50 ms map

105   window relative to stimulus onset, bandwidth of 20-35 Hz, pseudo-t = 0.3) consistent with the early

106   cortical component of visual evoked potentials[22] (Figure S1aviii). In addition to activation in occipital

107   cortex, SAM also revealed peaks associated with the visual network, including (aiii.) left optic tract (±75

108   ms map, 12-35 Hz bandwidth, pseudo-t = 0.4), (aiv.) left lateral geniculate n. (±50 ms map, 20-50 Hz

109   bandwidth, pseudo-t = 0.4), and (avii.) left superior colliculus (±50 ms map, 20-60 Hz, pseudo-t = 0.4.

110   Additional peaks were seen in (aii.) left anterior commissure (±75 ms map, 12-35 Hz bandwidth, pseudo-

111   t = 0.4), (av.) right posterior hippocampus (±75 ms map, 12-55 Hz bandwidth, both pseudo-t's = 0.3),

112   (avi.) right posterior white matter tracts (±75 ms map, 12-60 Hz bandwidth, pseudo-t = 0.4), and (ai.)

113   right arcuate cortex (±75 ms map, 12-120 Hz bandwidth, pseudo-t = 0.6.). Importantly, right arcuate and

114   left hippocampal responses were also detected in the LFP in response to visual stimulation (Figure S1b).

115   The visual stimulation experiment, in addition to serving as a positive control for evoked signals, also

116   demonstrates that SAM can localize primary sensory cortex in response to stimulation, that it can reveal

117   subcortical brain structures known to be involved in the processing of visual stimulation, and that

118   activated white matter tracts may also localized with SAM.

119

120   ***MEG Recordings of Stable Expression***

121   Eight weeks after transfection, and once the neural response to optical stimulation had reached a

122   plateau, MEG recordings commenced. Figure 2a depicts an example of optogenetic activation (50 ms

123   square pulses) in one NHP as localized by dual-state SAM to the posterior bank of the right arcuate

124   sulcus in the coronal (i), sagittal (ii), and axial planes (iii), as well as additional cortical peaks (local

125   maxima or minima in the SAM SPMs, Figure 2aii) near the site of optical stimulation. Peaks in the SAM

126   SPMs (local maxima or minima in the maps, here in units of pseudo-t scores) can be interpreted as

127   significant voxels in comparison to baseline and represent voxels of highly synchronous (red) or

128   desynchronous (blue) activity within the frequency band of interest. All brain images are depicted in

129   radiological coordinates, in which the right hemisphere is presented on the left. The whole brain, un-

130   thresholded, dual-state SAM SPM is depicted in Figure 2aiv; note the region of synchronized activity (red

131   voxels) arising from the site of activation and surrounded by desynchronized activity (blue voxels). For

132   Figures 2ai-iv, the dual-state beamforming parameters for the map were a ±75 ms window relative to

133   stimulus onset, for a frequency band of 15-35 Hz, and resulted in a pseudo-t score of 0.6. Figure 2b

134   depicts the SAM arcuate peaks corresponding to four additional and different optical stimulus inputs.

135   Figures 2bi-ii present peak activations in right arcuate for one NHP (same subject as in Figure 2a) and

136   Figures 2biii-iv shows right arcuate stimulation for a second NHP. Figure 2bi depicts the arcuate peak

137   (mapped at a ±3.5 s window relative to stimulus onset, bandwidth of DC-20 Hz, pseudo-t = 0.5) in

138   response to 8 Hz, sine waves (i.e., sinusoidal-modulation of the LED), and Figure 2bii shows the arcuate

139   peak in response to 40 Hz sine waves (±3.5 s map window, bandwidth of 20-50 Hz, pseudo-t = 0.7). The

140   results for arcuate stimulation in a second NHP are presented in Figures 2biii-iv; Figure 2biii shows the

141   SAM arcuate peak in response to 10 ms square wave pulses (±600 ms map, bandwidth of 3-70 Hz,

142   pseudo-t = 0.2), whereas Figure 2biv exhibits arcuate activity elicited by 20 Hz square wave pulse trains

143   (5 ms width for each square wave; ±200 ms map, bandwidth of 5-70 Hz, pseudo-t = 0.3). Details on the

144   stimuli and beamformer parameters for each stimulus type are presented in Methods. MSI can also be

145   used to construct virtual electrodes (source series) for any voxel in the brain, providing a continuous,

146   wide-band, sub-millisecond readout of activity that may provide similar neurophysiological data relative

147   to that resulting from an actual invasive electrode[7]. Figure 2bv presents a single trial of a local field

148   potential (white) recorded from the indwelling optrode and a simultaneous SAM virtual electrode (red,

149   viewing filters set from 1-30 Hz) extracted from the arcuate peak shown in Figure 2biii. The blue vertical

150   line indicates the time of stimulus onset, in this case a 10 ms square wave pulse. Both the LFP and virtual

151   electrode exhibit a rapid rise and peak in activity following stimulus onset, and both qualitatively share

152   similar features and time courses on a single trial basis.

153

154   Consistent activity was also elicited in the left hippocampi of two NHPs in response to a variety of optical

155   stimulus types. Figure 3a presents an example of the left SAM hippocampal peak co-localized to the site

156   of optical stimulation in a third subject, in this case a single, 60 s duration, 20 Hz sine wave. Figures 3ai-iii

157   depict the peak in the coronal (i), sagittal (ii), and axial planes (iii), and Figure 3aiv illustrates the un-

158   thresholded, whole-brain SAM dual state map (±4 s window, 10-30 Hz band, pseudo-t = 1.7) associated

159   with the 20 Hz sine wave input. Note the narrow band of synchronization (red) confined to the dorsal

160   aspect of the left hippocampus, and synchronous activity propagating towards left insula (e.g. see Figure

161   5a). The second row of Figure 3 depicts the left hippocampal peaks elicited by additional optogenetic

162   stimulation for two different NHPs. The first two coronal slices (Figures 3bi-ii) correspond to

163   hippocampal recordings obtained from a third NHP (same subject as presented in Figure 3a), and the

164   last two coronal slices depict activity for the first NHP, the latter for whose arcuate peaks were depicted

165   in Figure 2a. For Figure 3bi the stimulation parameters were single triangular (sawtooth) waves (±150

166   ms windows, 8-45 Hz band, pseudo-t = 0.8); for Figure 3bii the parameters were 10 ms square wave

167   pulses (±150 ms windows, bandwidth of 7-85 Hz, pseudo-t = 0.2). Figure 3bv presents a single trial of a

168   local field potential and the simultaneous SAM virtual electrode (viewing filters set from 1-35 Hz)

169   extracted from the hippocampal peak shown in Figure 3bi. The blue vertical line indicates the time of

170   the optical sawtooth onset. Both the LFP and virtual electrode exhibit a rapid rise and peak in activity

171   following stimulus onset, and both qualitatively share similar features and time courses on a single trial

172   basis. Hippocampal responses for the first NHP are depicted in Figure 3biii-iv with a hippocampal peak

173   elicited by 8 Hz sine waves (±2 s windows, DC-15 Hz band, pseudo-t = 1.0, Figure 3biii), and another

174   hippocampal peak elicited by 40 Hz sine waves (±2 s windows, 20-55 Hz band, pseudo-t = 0.6) shown in

175   Figure 3biv.

176

177   ***Functional Mapping***

178   In addition to eliciting biomagnetic activity at the transfection site, optogenetic stimulation also resulted

179   in propagation through well-described downstream networks. Because the SAM maps were constructed

180   for the whole brain volume, additional peaks were revealed in the various time-frequency SPMs.

181   Interestingly, right arcuate stimulation elicited additional SAM peaks in a pattern that conformed to a

182   known motor-associative network, the cortico-striatal-pallido-thalamocortical (CSPTC) motor

183   network[26,27]. This network was revealed in both NHPs who received arcuate stimulation across different

184   optical stimuli. An example of the CSPTC maps obtained for the first subject (as seen in Figure 2bi) are

185   shown in Figure 4a as a function of 8 Hz sine wave input. In addition to the activation of right arcuate

186   sulcus (ii), SAM maps also exhibited peaks in (i.) right anterior bank of the arcuate sulcus (±1 s windows,

187   DC-12 Hz band, pseudo-t = 0.3), (iii.) right corona radiata/ dorsolateral tip of the caudate n. (±4 s

188   windows, DC-15 Hz band, pseudo-t = 0.5), (iv.) right caudate n. (±2.5 s windows, DC-50 Hz band, pseudo-

189   t =0.7), (v.) right putamen/ external segment of globus pallidus (±4 s windows, DC-15 Hz band, pseudo-t

190   = 0.5), vi. and vii. posterior bank of contralateral (left) arcuate sulcus, coronal and sagittal slices,

191   respectively (±3 s windows, DC-15 Hz band, pseudo-t = 0.4), (viii.) right globus pallidus (±4 s windows,

192   DC-15 Hz band, pseudo-t = 0.4), (ix.) right ventroposterior medial / ventroposterior lateral n. of thalamus

193   (±4 s windows, DC-15 Hz band, pseudo-t = 0.4), (x.) right medial dorsal n. of thalamus (±4 s windows, DC-

194   15 Hz band, pseudo-t = 0.4), (xi.) ventral posterior thalamus (±3.5 s windows, DC-20 Hz band, pseudo-t =

195   0.3), and (xii.) parietal-occipital association area of the intraparietal sulcus (±2 s windows, DC-50 Hz

196   band, pseudo-t = 0.6). A second example of right hemispheric CSPTC network activity for a different NHP

197   in response to 20 Hz square wave pulse trains is presented in Figure 4b. Owing to the contrast of this

198   subject's MRI, the thalamic peak identities were less discernible. Despite this, SAM maps revealed peaks

199   in (i.) caudate n. (green, ±200 ms windows, 5-70 Hz band, pseudo-t = 0.3) and corona radiata (yellow,

200   ±200 ms windows, 5-70 Hz band, pseudo-t = 0.3), ii. thalamus (green, ±200 ms windows, 5-70 Hz band,

201   pseudo-t = 0.3) and caudate n. (yellow, ±200 ms windows, 5-70 Hz band, pseudo-t = 0.3), iii. posterior

202   dorsal bank of the arcuate sulcus (green, ±200 ms windows, 5-70 Hz band, pseudo-t = 0.3) and two

203   thalamic peaks (yellow, both ±200 ms windows, 5-70 Hz band, pseudo-t's = 0.3), iv. thalamus (±200 ms

204   windows, 5-70 Hz band, pseudo-t = 0.3), v. posterior ventral bank of arcuate sulcus (green, site of

205   stimulation, ±200 ms windows, 5-70 Hz band, pseudo-t = 0.3), corpus callosum (yellow, ±200 ms

206   windows, 5-70 Hz band, pseudo-t = 0.3), and caudate n. (yellow, ±200 ms windows, 5-70 Hz band,

207   pseudo-t = 0.3), vi. caudate n. (green, ±200 ms windows, 5-70 Hz band, pseudo-t = 0.3) and

208   mesencephalic nuclei (yellow, ±200 ms windows, 5-70 Hz band, pseudo-t = 0.3), vii. deep mesencephalic

209   n. (±200 ms windows, 5-70 Hz band, pseudo-t = 0.3), viii. substantia nigra (±200 ms windows, 5-70 Hz

210   band, pseudo-t = 0.3), ix. tegmental n. (±200 ms windows, 5-70 Hz band, pseudo-t = 0.3), x. pontine or

211   mesencephalic n. (±200 ms windows, 5-70 Hz band, pseudo-t = 0.3), and xi., and xii. all peaks in primary

212   motor cortex (area 4, ±300 ms windows, 4-70 Hz band, all pseudo-t's = 0.2).

213

214   Similarly, left hippocampal stimulation also elicited activity throughout the temporal network.

215   Functional hippocampal and temporal networks engaged by a 20 Hz optical sine input to left

216   hippocampus (as seen in Figures 3ai-iv) are shown for the third NHP in Figure 5a. Whole-brain SAM

217   SPMs for this stimulus exhibited peaks in the following areas: (i.) left insular proisocortex/temporopolar

218   proisocortex (±4 s windows, 10-30 Hz band, pseudo-t = 2.3), (ii.) left para-insular cortex (±4 s windows,

219   10-30 Hz band, pseudo-t = 2.4), (iii.) left dorsolateral amygdala (lateral n., ±4 s windows, 10-30 Hz band,

220   pseudo-t = 2.0), (iv.) left basolateral/lateral amygdala (±4 s windows, 10-30 Hz band, pseudo-t = 2.0), (v.)

221   left hippocampus, site of stimulation (±4 s windows, 10-30 Hz band, pseudo-t = 1.7), (vi.) left

222   parasubiculum/presubiculum of hippocampus (±4 s windows, 10-30 Hz band, pseudo-t = 1.6), (vii.)

223   contralateral (right) hippocampus (±4 s windows, 10-30 Hz band, pseudo-t = 2.6), and (viii.) left pontine

224   reticular activating formation (±4 s windows, 10-30 Hz band, pseudo-t = 2.0). A second example of

225   hippocampal network activity in a different NHP (as seen in Figure 3biii) in response to 8 Hz sine wave

226   input is presented in Figure 5b. The SAM peaks elicited by this stimulus are as follows: (i.) left insula (±2 s

227   windows, DC-15 Hz band, pseudo-t = 1.0), (ii.) PGa/IPa association areas of left temporal cortex (lateral

228   yellow peak, ±2 s windows, DC-15 Hz band, pseudo-t = 1.0), left hippocampus (green peak, site of

229   stimulation, ±2 s windows, DC-15 Hz band, pseudo-t = 1.0), and possible left red n. (yellow, medial peak,

230   ±2 s windows, DC-15 Hz band, pseudo-t = 0.6), (iii.) area TEA/TEM of left temporal cortex (±2 s windows,

231   DC-15 Hz band, pseudo-t = 1.0), and (iv.) area TL/TFM of right temporal cortex (±2 s windows, DC-15 Hz

232   band, pseudo-t = 0.9). A third example of hippocampal network activity in response to 40 Hz sine wave

233   input (same subject as in Figure 5b) is presented in Figure 5c. The SAM peaks are as follows: (i.) left

234   anterior hippocampus (±1.5 s windows, 20-50 Hz band, pseudo-t = 0.9), (ii.) left hippocampus, site of

235   stimulation (±2 s windows, 20-55 Hz band, pseudo-t = 0.6), (iii.) possible left deep mesencephalic n. (±2 s

236   windows, 20-55 Hz band, pseudo-t = 0.7), and (iv.) left pulvinar n. of thalamus (±1.5 s windows, 20-50 Hz

237   band, pseudo-t = 0.4). Collectively, these results indicate the utility of combining optogenetic techniques

238   with MEG for functional brain mapping and mapping of deep structures, even under anesthesia.

239

240   **DISCUSSION**

241

242 This study represents the first successful combination of optogenetics with magnetic source imaging of

243 biomagnetic signals in non-human primates, and provides additional information on the relationship

244 between MEG signals and the underlying electrical activity in the brain[28]. In this study, we have

245 demonstrated anatomically-localized and temporally-precise control over neural activity in a MEG-

246 compatible optogenetic preparation.

247

248 We provide evidence of the feasibility of optogenetic stimulation in the MEG environment and show

249 that after optogenetic stimulation, both arcuate cortex and hippocampus can be localized by MSI across

250 multiple NHPs, across stimulus types, and at a voxel size of 750 μm^3. In addition, SAM can be used

251 localize activity to NHP occipital cortex in response to visual stimulation. While the amplitude of the

252 localized signal (as given by SAM pseudo-t score) varies, this is likely due to the type of stimulus input

253 and can be used in the future to examine the effects of different time-varying inputs into a target

254 structure. This study also provides evidence that a signal generated in deep brain structures is

255 detectable with MEG, including hippocampus, and that downstream activation of other structures such

256 as amygdala, caudate nucleus, putamen, globus pallidus, thalamic nuclei, superior colliculus, and even

257 white matter is also detectable. Detection is possible even in the presence of high noise and suboptimal

258 conditions resulting from the experimental preparation (e.g., the small size of the vervet brain, a large

259 heartbeat artifact, artifact from anesthesia monitoring equipment, etc.).

260

261 Studies using non-human primates in MEG have previously demonstrated the feasibility of equivalent

262 current dipole[32] and beamformer[33] analyses in monkeys. This study extends these observations to

263 analysis of areas beyond superficial cortex into deep structures in an NHP species with a smaller brain,

264 strongly supporting the validity of MSI in detecting deep brain signals. Furthermore, this study uses

265   experimentally controlled, optogenetically generated signals from a known source and onset time to

266   demonstrate the accuracy of localization. The current results suggest that a combination of whole head

267   coverage with axial gradiometers, a low noise floor, low head movement, and appropriate use of

268   beamformers allows deep localization of activity that is consistent with theoretical investigations and

269   data from epilepsy patients[2–5,8,11]. SAM normalizes MEG signals with respect to the noise in the unique

270   recording environment and with distance from the sensors; therefore, deep signals are localizable given

271   sufficient signal-to-noise ratio (SNR). SNR amplification in this study was achieved through repeated

272   presentations of the stimuli, by low head motion, and by beamforming itself, which also removes noise[7].

273

274   The relevance of this finding to the clinical evaluation of epilepsy surgery candidates is significant.

275   Currently, MEG is FDA approved for pre-surgical evaluation of epilepsy, but is often limited to dipole

276   analyses only[16,34,35]. Unfortunately, dipole analyses break down with low SNR[5], which is often the case

277   with deep signals. The most common epilepsy type requiring surgical resection is mesial temporal lobe

278   epilepsy wherein the seizure generator is deep in the brain[36], thus methods permitting the localization

279   of deep signals with MEG in such patients is of great utility in surgical planning. To this point, our results

280   demonstrate that SAM can accurately localize a deep signal to its source (hippocampus). Furthermore,

281   while Mikuni et. al. estimated 4 cm^2 of active brain tissue is required for the localization of spikes[13], our

282   results show that significantly less tissue may be required to generate a detectable MEG signal, simply

283   because the vervet hippocampus is far smaller, as are the structures comprising the CSPTC and visual

284   networks. Additionally, the injection parameters of our viral vector[37-39] and microscopy suggest that the

285   volume activated was only a few mm^3, and while it is likely that feed forward activation occurs we

286   suspect that this falls well below 4 cm^2 of tissue (see Figures 1ai, bi; Figure 3aiv, for examples).

287

288   The results of this study suggest that optogenetics can be combined with MEG imaging in non-human

289   primates to permit precise functional mapping. Stimulation of arcuate sulcus activated the cortico-

290   striato-pallido-thalamo-cortical (CSPTC) network such that voxels of peak activation fell within a

291   functionally and anatomically described pathway[26,27]. Further, hippocampal stimulation evoked

292   widespread activity in regions such as amygdala, insula, and contralateral hippocampus. Finally, natural

293   visual stimulation using flashes of light elicited activity throughout the visual system. In the future, the

294   combination of optogenetic techniques with MEG/MSI could be used to variably activate or inactivate

295   discrete parts of the brain with excitatory or inhibitory opsins to reveal functional relationships that

296   have not previously been described.

297

298   The temporal resolution of MEG enables this combination of techniques to map transient interactions

299   that are not detectable using other functional imaging approaches[40]. Recent analysis techniques

300   designed to increase fMRI sampling rate (e.g. dynamic functional magnetic resonance inverse imaging[41]),

301   have achieved a maximum sampling rate around 10 Hz with a 5 mm^3 voxel size[42,43] with the 10 Hz period

302   corresponding to events lasting 100 ms. In contrast, arcuate cortex was stimulated with trials of 50 ms

303   square wave inputs and beamforming revealed arcuate peaks at 75 ms, and with a voxel size of 750 μm^3

304   (Figure 2a), and 50 ms flashes of light elicited SAM peaks at 50 ms in occipital cortex (Figure S1aviii).

305   These fast-transient events occur well beyond the temporal resolution of metabolically based methods

306   and the recruitment of downstream areas can happen rapidly, suggesting that functional maps and

307   connectivity analyses will vary depending on the duration and sampling rate of analyzed data. For

308   example, fMRI network architecture has been demonstrated to change over short timescales

309   (hours/minutes) during learning[44], while analysis of MEG based network architecture has demonstrated

310   variability on the order of milliseconds[45]. It is clear from this demonstration that the high sampling rates

311   of MEG coupled with SAM affords exceptional advantages over traditional neuroimaging techniques.

312   However because the beamformer problem is without a unique solution there will always be inherent

313   uncertainties in localization[46] without "ground truth" experiments utilizing controlled inputs to known

314   brain targets. To this end, the approach we report may assist in efforts to continually to improve inverse

315   problem solutions to yield greater certainty[30,47].

316

317   In addition to the measurement of functional circuits, optogenetic control of neuronal field potentials

318   combined with MEG will make it possible to investigate relationships that exist due to specific, transient

319   activity patterns. For example, it may be possible to capture native activity at a recording site, use

320   optogenetic stimulation to approximate population activity, and map the resultant response irrespective

321   of state or behavior[48]. We anticipate that experimenter control over discrete brain regions of interest

322   coupled to whole brain recording and detection of downstream responders will provide a platform for

323   improved investigation of brain function in both normal and pathological conditions. Subthreshold

324   modulation could be used to investigate population activity that gives rise to neural oscillations[49,50] and

325   suprathreshold synchronous modulation could be used to mimic epileptiform discharges in the study of

326   epilepsy[50].

327

328   The results of this study support, through direct measurement, the assumed theoretical ability of

329   MEG/MSI to detect and localize experimentally controlled activity in the brain at very fine temporal and

330   spatial resolution. We have demonstrated the feasibility of localizing activity in the brains of vervet

331   monkeys using whole head instrumentation designed for human subjects. By combining optogenetic

332   stimulation in MEG with beamformer analysis it is possible to empirically determine the practical

333   abilities and limitations of MEG/MSI. Additionally, it is clear that this combination of techniques may

334   permit functional brain mapping in spatial and temporal domains not otherwise possible with current

335   functional imaging techniques.

336

350

ONLINE METHODS

352

Surgical Targeting

All studies were approved by the Animal Care and Use Committee of Wake Forest School of Medicine.

This study was repeated in three female vervet monkeys, *Chlorocebus aethiops*, aged 15-16 years and

weighing between 4.99-6.75 kg. Each animal was mounted in an MRI compatible stereotaxic frame with

lipid containing ear bars, and T1-weighted anatomical images were acquired using a 3D-MPRAGE 0.5

mm isotropic sequence in a Siemens 3 T Skyra system with a custom built 8-channel flexible head coil

(Dr. Cecil Hayes, Univ. Washington). The animals were removed from the stereotaxic frame and an

360   additional structural MRI scan was acquired in which the animals were fitted with three lipid biomarkers

361   fixed in the location of the MEG fiducials (placed in the conventional three-point fiducial locations) for

362   co-registration with MEG data. The locations of the MEG fiducials were tattooed on the animals prior to

363   the start of the study to ensure precise co-registration across multiple sessions. In one animal a post-

364   mortem MRI was conducted after implantation and recording to confirm stereotaxic targeting (Figures.

365   1aii-iii and bii-iii).

366

367   Using Medical Image Processing, Analysis, and Visualization (MIPAV) software available from the NIH,

368   stereotaxic coordinates were generated for CA3 of left hippocampus and for the posterior wall of the

369   contralateral, right arcuate sulcus.

370

371   ***Surgery***

372   Animals were securely mounted and centered in a surgical stereotaxic frame. The cranium was exposed

373   and ten ceramic screws (Rogue Research Inc.; Montreal, Canada) were placed around the perimeter of

374   the surgical margin. A craniotomy (~17 mm) was then drilled over the coordinates for each targeted

375   brain region. A custom polyether ether ketone (PEEK) cannula with a Teflon stop was advanced through

376   the dura on a stainless steel stylette. The stylette was retracted leaving the cannula in place; injection of

377   the viral vector and placement of the optrode (optical fiber and recording electrode) was done through

378   the cannula to ensure co-localization. A gas-tight, micro volume Hamilton Syringe was then filled with

379   AAV10-CaMKIIa-ChR2-eYFP (provided by Dr. Caroline Bass, SUNY Buffalo) and 4 μL of virus was injected

380   at each coordinate through a 38 G needle at a rate of 0.5 μL/minute. The syringe was left in place for 5

381   minutes following the injection and slowly removed. A custom made, chronically indwelling optrode was

382   implanted to a depth of 0.5 mm above the injection coordinates. The optrode consisted of either a 200

383   or 400 μm diameter fiber optic cable (ThorLabs, Inc.; Newton, NJ) coupled to a 75 μm Pt/Ir electrode

384   (FHC, Inc.; Bowdoin, ME) or a 35 μm formvar-coated Tungsten electrode (California Fine Wire Co.;

385   Grover Beach, CA), which extended 0.7 mm beyond the tip of the optical fiber. Lastly, a custom (PEEK)

386   headwell with a removable cap (Crist Instruments Co., Inc.; Bethesda, MD) was fitted over each

387   craniotomy and cemented in place. The craniotomy was sealed with bone cement securing the optrode

388   in place.

389

390   To ensure electrical and magnetic silence, we avoided the photovoltaic effect by designing optrodes

391   with a beveled tip so that the conductive surface was in shadow rather than in the cone of light[22–24]. The

392   absence of artifact was confirmed in saline and in pre-expression control recordings.

393

394   *Control for Photoelectric Effects*

395   Prior to implantation, a combined fiberoptic/recording electrode (optrode) was submerged in saline and

396   LED stimulation was conducted to rule-out artifacts associated with the photovoltaic effect. No transient

397   artifact associated with the LED was detected upon stimulation and there was no significant difference

398   in LFP amplitude from the pre-stimulation period suggesting the optrode design used was not

399   susceptible to the photovoltaic effect.

400

401   *Electrophysiology Recordings*

402   Recordings were conducted under anesthesia, using propofol (200-400 μg/kg/min) for the MEG scans

403   and ketamine (12-15 mg/kg) and dexmedetomidine (0.0075-0.015 mg/kg) for the electrophysiological

404   recordings. MEG recordings were conducted in a magnetically shielded room (MSR; Vacuumschmelze

405   GmbH & Co.; Hanau, Germany) with a CTF MEG^{TM} whole cortex helmet equipped with 275 first-order

406   axial gradiometer coils, each with a 5 cm baseline and 22.4 mm average inter-sensor spacing and 29

407   reference sensors (CTF MEG International Services Limited Partnership; Coquitlam, BC, Canada). MEG

408   recordings were sampled at 2400 Hz for a bandwidth of DC-600 Hz. Data were powerline filtered offline

409   for 60 Hz harmonics with a 4 Hz width, and synthetic third order gradiometry was applied.

410   Simultaneously recorded LFP data were amplified using a Nicolet intraoperative monitoring system

411   (Natus Medical; Pleasanton, CA) sampled at 5 kHz with maximum range of +/- 5 mV with a bandpass

412   filter of 0.1 Hz to 3 kHz and recorded in line with MEG data. On separate days without MEG recordings,

413   LFP data were recorded using a SciWorks recording system (DataWave Technologies; Loveland, CO), AM-

414   3600 extracellular amplifiers (A-M Systems; Carlsborg, WA), and a T8G100 headstage amplifier (Triad

415   Biosystems International; Durham, NC) and bandpass filtered at 0.3 Hz to 5 kHz, with a gain of 500 and a

416   40 kHz sampling rate.

417

418   Prior to the optrode implantation, 8-minute resting-state MEG scans were acquired to establish baseline

419   activity. Two weeks after surgery (before high level transgene expression, and after the animal had

420   recovered from surgery) animals were stimulated for the first time at a range of optical intensities (10.3-

421   75.6 mW/mm^2 for 200 μm and 2.6-18.9 mW/mm^2 for 400 μm fiber). These recordings were conducted

422   in the MEG MSR under anesthesia as described, as well as in separate sessions in a dedicated

423   electrophysiology suite. A variety of optical stimuli were delivered, including single 10 ms or 50 ms

424   square pulses of 473 nm light from either a light emitting diode (ThorLabs) or from a laser (Shanghai

425   Dream Laser Technology Co., Ltd; Song Jiang, Shanghai, China), 20 Hz square wave pulse trains, single

426   triangular (sawtooth) ramps, and sine waves at 8, 20, or 40 Hz (see below for more stimulus details).

427   Pulse duration of the laser was controlled with a 2 mm Uniblitz laser shutter and a D880C Uni-stable

428   driver (Uniblitz Electronic; Rochester, NY). LED pulse durations were controlled with custom MATLAB

429   scripts (Natick, Massachusetts: The MathWorks Inc.) and a digital-analog converter (DAC; Data

430   Translation, Inc.; Marlborough, MA). After stable transgene expression was determined, the animals

431   were stimulated again using the same paradigms as above and the resulting activity was recorded.

432   Electrophysiological and MEG recordings after stable expression were again done simultaneously using

433   the Nicolet system for acquiring electrophysiology during MEG and also separately.

434

435   The optrodes were tested in saline prior to implantation; *in vitro* two weeks after transfection; as well as

436   post mortem. As a positive control for the electrode and MSI, analysis of visual stimulation was

437   conducted. One hundred nineteen, 50 ms pulses of white light were presented via fiber optic cable to

438   the left lower quadrant of the visual field of the left eye of the sedated animal. The right eye was taped

439   shut per typical recording protocol while the left eye remained open. The fiber optic cable was

440   channeled into the helmet slightly lateral and inferior to the left eye. The light pulses had a 3 s ISI via

441   LED, and the experiment was performed in both the electrophysiology suite and in the MEG MSR.

442   Timing was controlled by custom MATLAB scripts.

443

444   ***Analysis***

445   All analyzed data were derived from recordings in which motion was no greater than 0.2 mm. Head

446   motion was nearly eliminated through the use of anesthesia and a carefully supported head.

447

448   Data preprocessing, head model creation, and beamforming were performed using CTF MEG[TM] Software

449   (CTF MEG International Services Limited Partnership, Coquitlam, BC, Canada). MEG preprocessing

450   included DC-offsetting, application of synthetic third order gradiometry, and powerline filtering[7]. MEG

451   data were then co-registered with the monkey's anatomical MRI data using the standard three-point

452   fiducials. From this, a multiple-overlapping-spheres model of the head and whole brain volume was

453   generated[25]. Dual-state SAM[3,5] was applied to each active time segment and an equal length control

454   segment composed of data preceding the stimulus, to construct 3D images of the entire brain volume.

455   Noise normalized t-deviate statistical parametric maps of source power were derived from the

456   beamformer output at a voxel size ranging from 0.75 - 1.5 mm³. Results are shown for 750 μm³ analyses

457   due to superior accuracy in source localization. Such small voxel sizes were possible because of

458   extremely low motion associated with this preparation. The degree of activation in each voxel is

459   indicated by a pseudo t-score. Local maxima (synchronization) and minima (desynchronization) of the

460   SAM maps were identified as voxels of peak activity.

461

462   SAM time-frequency analysis parameters were determined in part by the time-frequency characteristics

463   of the input stimulus and by the power spectral densities (PSDs) and timing of the neural response

464   measured on the LFP during simultaneous MEG/LFP recordings in the MSR when such recordings were

465   obtained. In general, for brief stimuli, the beamforming windows necessary to detect activity changes

466   also needed to be short, with a correspondingly wider frequency band to provide enough samples for

467   analysis. For the sine wave inputs, the SAM frequency bands were set to bracket the sine frequency, and

468   because the sine inputs were of longer duration the beamforming windows were correspondingly

469   longer, both to provide enough samples for the analysis and also because the brain circuits appeared to

470   sustain activity for a long time (see Results). Specific arcuate beamforming parameters for each stimulus

471   type are as follows. For the 50 ms square pulses (120 trials, 5 s ISI), dual-state SAM relative to stimulus

472   onset was conducted in 50 ms steps from 100-500 ms inclusive and for another window of 75 ms

473   (Figures 2ai-iv). For each time window, the high-pass was set above the threshold for aliasing and the

474   low-passes were varied in a series of 10 Hz steps ranging from 40-100 Hz and another step at 35 Hz.

475   Peak voxels were identified in each whole-brain, time-frequency map and because peak voxels often

476   appeared in multiple maps the time-frequency combination that expressed the maximal pseudo-t score

477   for each peak was chosen as the representative map. A primate neuroanatomist (J.D.) confirmed the

478   neuroanatomic localizations of the peaks to their target structures and also for downstream structures

479   that were also activated following stimulation. For the 8 Hz sine waves (3 s stimulus length, 20 trials, 10

480   s ISI, Figure 2bi) the SAM time-frequency parameters were 1-4 s windows in 500 ms steps, a DC high-

481   pass, and low-pass steps of 12, 15, 20, and 50 Hz. For the 40 Hz sine waves (3 s stimulus length, 20 trials,

482   10 s ISI, Figure 2bii) the SAM parameters were 500 ms - 4 s windows in 500 ms steps, a high-pass series

483   ranging from 10-35 Hz in 5 Hz steps, and low-pass steps at 50 and 55 Hz. For the 10 ms square pulses

484   (100 trials, 6 s ISI, Figure 2biii), SAM was conducted in 50 ms steps for windows from 100-750 ms, plus

485   additional windows at 125 ms and 1 s, while the frequency bands had a minimum high-pass set to

486   prevent aliasing for each time window, and a low-pass set at 50, 70, and 100 Hz. For the 20 Hz square

487   pulse train (5 ms width squares, 10 pulses/train, 100 trains, 6 s ISI, Figure 2biv) the SAM time frequency

488   parameters included windows from 100-500 ms conducted in 100 ms steps, plus an extra window at 750

489   ms, a high-pass set to prevent aliasing for each window, and a low-pass at either 70 or 100 Hz.

490

491   Beamforming parameters for the hippocampal stimulation experiments are as follows. For the single 60

492   s, 20 Hz sine wave (5 V, Figure 3ai-iv) the dual-state SAM time windows were 2, 3, 4, 5, 10, 20, 30, and

493   60 s, the high-pass was either 10 or 15 Hz, and the low-pass was 30 Hz. For the single sawtooth ramps

494   (150 ms duration, 20 trials at an intensity of 4.996 V and 9.528 W, 6 s ISI, Figure 3bi) the SAM

495   parameters included 150-400 ms time windows in 50 ms steps, plus additional windows at 125 ms and

496   500 ms, a high-pass set to prevent aliasing per time window, and low-passes ranging from 40-55 Hz in 5

497   Hz steps, plus additional windows at 70, 100, and 120 Hz, plus at 35 Hz for windows of sufficiently long

498   duration. For the 10 ms square pulse stimuli (114 trials, 4.996 V/9.28 W, 6 s ISI, Figure 3bii) the SAM

499   time-frequency parameters included 50, 175 ms windows, in 25 ms steps, a high-pass set to prevent

500   aliasing per time window, and low-passes ranging from 30-100 Hz (when the time window permitted a

501   small low pass) in 5 Hz steps, with additional windows at 120 and 200 Hz. For the 8 Hz sine waves (3 s

502   duration, 20 trials, 10 s ISI, Figure 3biii) the beamforming parameters included 1-3 s windows in 500 ms

503   steps, a DC high-pass, and a low-pass of 12, 15, or 20 Hz. For the 40 Hz sine waves (3 s duration, 20 trials,

504   10 s ISI, Figure 3biv) the beamforming parameters included 1-3 s windows in 500 ms steps, high-passes

505   of 10, 20, 30 or 35 Hz, and low-passes of 50, 55, or 60 Hz.

506

507   Beamforming for the visual stimulation experiment (Figure S1) included 50-300 ms windows in 25 ms

508   steps, a high-pass set to prevent aliasing per time window, and low-passes ranging from 30-70 Hz in 5 Hz

509   steps, plus additional windows at 80, 90, 100, 120, and 200 Hz.

510

511   LFP data were analyzed using SciWorks, Neuroexplorer (Nex Technologies, Madison, Al), and custom

512   scripts in MATLAB. Peak amplitude of the LFP in response to optical stimulation during electrophysiology

513   recordings was measured between two-week, five-week, and seven-week time points.Peak amplitudes

514   for each replicate were measured at the time point corresponding to the peak of the average trace for

515   each light intensity.

516

517   ***Histology***

518   To confirm the anatomical position of the optrode placement and injection site, at the completion of the

519   imaging study, one animal was necropsied by first sedating with ketamine followed by an overdose with

520   pentobarbital. A thoracotomy was conducted and the animal was transcardially perfused with ice-cold

521   phosphate buffered saline followed by 4% paraformaldehyde fixative. The brain was extracted and

522   sectioned at a 50 µm thickness on a modified Vibratome 1000 (Leica Biosystems Inc.; Buffalo Grove, IL).

523   Sections of tissue were mounted on gelatin coated microscope slides and imaged on a Zeiss LSM 710

524   confocal microscope with 10X and 20X objectives (Carl Zeiss Microscopy, LLC; Thornwood, NY).

525

526   **REFERENCES**

527   1.   Nasiotis, K., Clavagnier, S., Baillet, S. & Pack, C. C. High-resolution retinotopic maps estimated with

528   magnetoencephalography. *NeuroImage* doi:10.1016/j.neuroimage.2016.10.017

529   2.   Vrba, J. & Robinson, S. E. Signal Processing in Magnetoencephalography. *Methods* **25,** 249–271

530   (2001).

531   3.   Robinson, S. & Vrba, J. Functional Neuroimaging by Synthetic Aperture Magnetometry. in *11th Int.*

532   *Conf. on Biomagnetism* (1998).

533   4.   Vrba, J., Robinson, S. E. & McCubbin, J. How many channels are needed for MEG? *Neurol. Clin.*

534   *Neurophysiol. NCN* **2004,** 99 (2004).

535   5.   Hillebrand, A. & Barnes, G. R. in (ed. Neurobiology, B.-I. R. of) **68,** 149–171 (Academic Press, 2005).

536   6.   Troebinger, L. *et al.* High precision anatomy for MEG. *NeuroImage* **86,** 583–591 (2014).

537   7.   Stapleton-Kotloski, J. R. *et al.* Localization of interictal epileptiform activity using

538   magnetoencephalography with synthetic aperture magnetometry in patients with a vagus nerve

539   stimulator. *Brain Imaging Methods* **5,** 244 (2014).

540   8.   Robinson, S., Nagarajan, S., Mantle, M., Gibbons, V. & Kirsch, H. Localization of Interictal Spikes

541   using SAM(g2) and Dipole Fit. *Neurol. Clin. Neurophysiol. NCN* **2004,** 74 (2004).

542   9.   Ukai, S. *et al.* SAM(g2) analysis for detecting spike localization: a comparison with clinical symptoms

543   and ECD analysis in an epileptic patient. *Neurol. Clin. Neurophysiol. NCN* **2004,** 57 (2004).

544   10. Ishii, R. *et al.* Spatially filtered magnetoencephalography compared with electrocorticography to

545   identify intrinsically epileptogenic focal cortical dysplasia. *Epilepsy Res.* **81,** 228–232 (2008).

546   11. Cornwell, B. R., Johnson, L. L., Holroyd, T., Carver, F. W. & Grillon, C. Human hippocampal and

547   parahippocampal theta (θ) during goal-directed spatial navigation predicts performance on a virtual

548   Morris water maze. *J. Neurosci. Off. J. Soc. Neurosci.* **28,** 5983–5990 (2008).

549   12. Cornwell, B. R. *et al.* Evoked amygdala responses to negative faces revealed by adaptive MEG

550   beamformers. *Brain Res.* **1244,** 103–112 (2008).

551 13. Mikuni, N. *et al.* Simultaneous Recording of Epileptiform Discharges by MEG and Subdural

552   Electrodes in Temporal Lobe Epilepsy. *NeuroImage* **5,** 298–306 (1997).

553 14. Baumgartner, C., Pataraia, E., Lindinger, G. & Deecke, L. Neuromagnetic recordings in temporal lobe

554   epilepsy. *J. Clin. Neurophysiol.* **17,** 177–189 (2000).

555 15. Shigeto, H. *et al.* Feasibility and limitations of magnetoencephalographic detection of epileptic

556   discharges: Simultaneous recording of magnetic fields and electrocorticography. *Neurol. Res.* **24,**

557   531–536 (2002).

558 16. Kharkar, S. & Knowlton, R. Magnetoencephalography in the presurgical evaluation of epilepsy.

559   *Epilepsy Behav.* **46,** 19–26 (2015).

560 17. Boyden, E. S., Zhang, F., Bamberg, E., Nagel, G. & Deisseroth, K. Millisecond-timescale, genetically

561   targeted optical control of neural activity. *Nat Neurosci* **8,** 1263–1268 (2005).

562 18. Han, X. in *Progress in Brain Research* **196,** 215–233 (Elsevier, 2012).

563 19. Cardin, J. A., Kumbhani, R. D., Contreras, D. & Palmer, L. A. Cellular mechanisms of temporal

564   sensitivity in visual cortex neurons. *J. Neurosci. Off. J. Soc. Neurosci.* **30,** 3652–3662 (2010).

565 20. Klorig, D. C. & Godwin, D. W. A magnetic rotary optical fiber connector for optogenetic experiments

566   in freely moving animals. *J. Neurosci. Methods* **227,** 132–139 (2014).

567 21. Huang, M. X., Mosher, J. C. & Leahy, R. M. A sensor-weighted overlapping-sphere head model and

568   exhaustive head model comparison for MEG. *Phys. Med. Biol.* **44,** 423 (1999).

569 22. Di Russo, F., Martínez, A., Sereno, M. I., Pitzalis, S. & Hillyard, S. A. Cortical sources of the early

570   components of the visual evoked potential. *Hum. Brain Mapp.* **15,** 95–111 (2002).

571 23. Belmalih, A. *et al.* A multiarchitectonic approach for the definition of functionally distinct areas and

572   domains in the monkey frontal lobe. *J. Anat.* **211,** 199–211 (2007).

573 24. BrainMaps.org - Interactive Brain Atlas, Neuroanatomy, Brain Mapping. Available at:

574   http://brainmaps.org/ajax-

575   viewer.php?datid=42&sname=220&hname=arcuate%20sulcus&hlabel=AS. (Accessed: 21st

576   September 2016)

577   25. Woods, R. P. *et al.* A web-based brain atlas of the vervet monkey, Chlorocebus aethiops.

578   *NeuroImage* **54,** 1872–1880 (2011).

579   26. Worbe, Y., Lehericy, S. & Hartmann, A. Neuroimaging of tic genesis: Present status and future

580   perspectives. *Mov. Disord.* **30,** 1179–1183 (2015).

581   27. Worbe, Y. *et al.* Altered structural connectivity of cortico-striato-pallido-thalamic networks in Gilles

582   de la Tourette syndrome. *Brain* **138,** 472–482 (2015).

583   28. Ioannides, A. A. Magnetoencephalography as a research tool in neuroscience: state of the art.

584   *Neurosci. Rev. J. Bringing Neurobiol. Neurol. Psychiatry* **12,** 524–544 (2006).

585   29. Buzsáki, G., Anastassiou, C. A. & Koch, C. The origin of extracellular fields and currents--EEG, ECoG,

586   LFP and spikes. *Nat. Rev. Neurosci.* **13,** 407–420 (2012).

587   30. Jonmohamadi, Y. & Jones, R. D. Source-space ICA for MEG source imaging. *J. Neural Eng.* **13,** 016005

588   (2016).

589   31. Bauer, M., Trahms, L. & Sander, T. Magnetoencephalographic accuracy profiles for the detection of

590   auditory pathway sources. *Biomed. Eng. Biomed. Tech.* **60,** 135–145 (2014).

591   32. Wilson, T. W. *et al.* A MEG investigation of somatosensory processing in the rhesus monkey.

592   *NeuroImage* **46,** 998–1003 (2009).

593   33. Zumer, J. M. *et al.* MEG in the macaque monkey and human: Distinguishing cortical fields in space

594   and time. *Brain Res.* **1345,** 110–124 (2010).

595   34. Kaiboriboon, K., Nagarajan, S., Mantle, M. & Kirsch, H. E. Interictal MEG/MSI in intractable mesial

596   temporal lobe epilepsy: Spike yield and characterization. *Clin. Neurophysiol.* **121,** 325–331 (2010).

597   35. Bagić, A. I., Knowlton, R. C., Rose, D. F. & Ebersole, J. S. American Clinical Magnetoencephalography

598   Society Clinical Practice Guideline 1: Recording and Analysis of Spontaneous Cerebral Activity*. *J.*

599   *Clin. Neurophysiol.* 1 (2011). doi:10.1097/WNP.0b013e3182272fed

600   36. Giulioni, M. *et al.* Seizure outcome in surgically treated drug-resistant mesial temporal lobe epilepsy

601   based on the recent histopathological classifications: Clinical article. *J. Neurosurg.* 1–11 (2013).

602   37. Han, X. *et al.* Millisecond-Timescale Optical Control of Neural Dynamics in the Nonhuman Primate

603   Brain. *Neuron* **62,** 191–198 (2009).

604   38. Watakabe, A. *et al.* Comparative analyses of adeno-associated viral vector serotypes 1, 2, 5, 8 and 9

605   in marmoset, mouse and macaque cerebral cortex. *Neurosci. Res.* **93,** 144–157 (2015).

606   39. Davidson, B. L. & Breakefield, X. O. Viral vectors for gene delivery to the nervous system. *Nat. Rev.*

607   *Neurosci.* **4,** 353–364 (2003).

608   40. Lin, P., Fang, Z., Liu, J. & Lee, J. H. Optogenetic Functional MRI. *J. Vis. Exp. JoVE* (2016).

609   doi:10.3791/53346

610   41. Lin, F.-H., Witzel, T., Zeffiro, T. A. & Belliveau, J. W. Linear constraint minimum variance beamformer

611   functional magnetic resonance inverse imaging. *NeuroImage* **43,** 297–311 (2008).

612   42. Lin, F.-H. *et al.* Increasing fMRI Sampling Rate Improves Granger Causality Estimates. *PLOS ONE* **9,**

613   e100319 (2014).

614   43. Lin, F.-H. *et al.* Ultrafast inverse imaging techniques for fMRI. *NeuroImage* **62,** 699–705 (2012).

615   44. Bassett, D. S. *et al.* Dynamic reconfiguration of human brain networks during learning. *Proc. Natl.*

616   *Acad. Sci.* **108,** 7641–7646 (2011).

617   45. Fatima, Z., Kovacevic, N., Misic, B. & McIntosh, A. R. Dynamic functional connectivity shapes

618   individual differences in associative learning. *Hum. Brain Mapp.* n/a-n/a (2016).

619   doi:10.1002/hbm.23285

620   46. Hillebrand, A., Singh, K. D., Holliday, I. E., Furlong, P. L. & Barnes, G. R. A new approach to

621   neuroimaging with magnetoencephalography. *Hum. Brain Mapp.* **25,** 199–211 (2005).

622   47. Huang, M.-X. *et al.* MEG source imaging method using fast L1 minimum-norm and its applications to

623   signals with brain noise and human resting-state source amplitude images. *NeuroImage* **84,** 585–

624   604 (2014).

625   48. Hass, C. A. & Glickfeld, L. L. High fidelity optical excitation of cortico-cortical projections at

626   physiological frequencies. *J. Neurophysiol.* jn.00456.2016 (2016). doi:10.1152/jn.00456.2016

627   49. Duffy, B. A., Choy, M., Chuapoco, M. R., Madsen, M. & Lee, J. H. MRI compatible optrodes for

628   simultaneous LFP and optogenetic fMRI investigation of seizure-like afterdischarges. *NeuroImage*

629   **123,** 173–184 (2015).

630   50. Klorig, D. C., Alberto, G. E., Smith, T.,& Godwin, D. W. Optogenetically-induced population discharge

631   threshold as a sensitive measure of network excitability. *ENEURO* **6**(6) 1-16 (2019).

632   doi:10.1523/ENEURO.0229-18.2019.

633

634

635

636

637
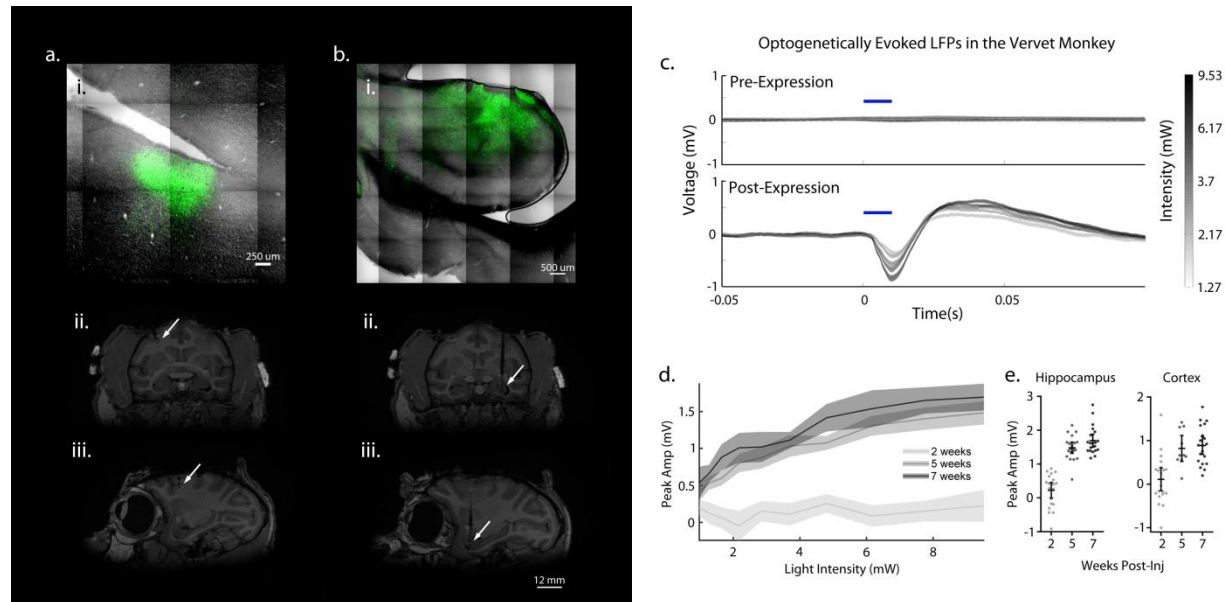
Figure 1. Location of optogenetic protein expression and light evoked responses. ai. ChR2-eYFP labeled neurons confined to gray matter of the posterior wall of right arcuate sulcus corresponding to area 8a, white line indicates approximate boundary between gray and white matter. Coronal (**ii**) and sagittal (**iii**) MRI demonstrating colocalization of the optrode. **bi**. ChR2-eYFP labeled neurons in the anterior dorsolateral aspect of left hippocampus corresponding to area CA3 indicate transgene expression. Coronal (**ii**) and sagittal (**iii**) MRI demonstrating colocalization of the optrode. **c.** Example of averaged response to stimulation at five intensity levels (grey to black) in hippocampus showing absence of response in week 2 (upper trace) compared to the large, biphasic LFP in week 7 (lower trace). Blue bar indicates stimulus onset and duration. **d.** Average intensity-response curves for each of the three time points. Bands = 95% CI. **e.** Maximum intensity stimulation (9.53 mW) of cortex and hippocampus at 7 weeks post transfection elicited a response as measured by the LFP electrode that was greater than at 2 weeks post-transfection. AS= arcuate sulcus; GM= gray matter; WM = white matter; DG= dentate gyrus; SB= subiculum.

644

645

646

647

648
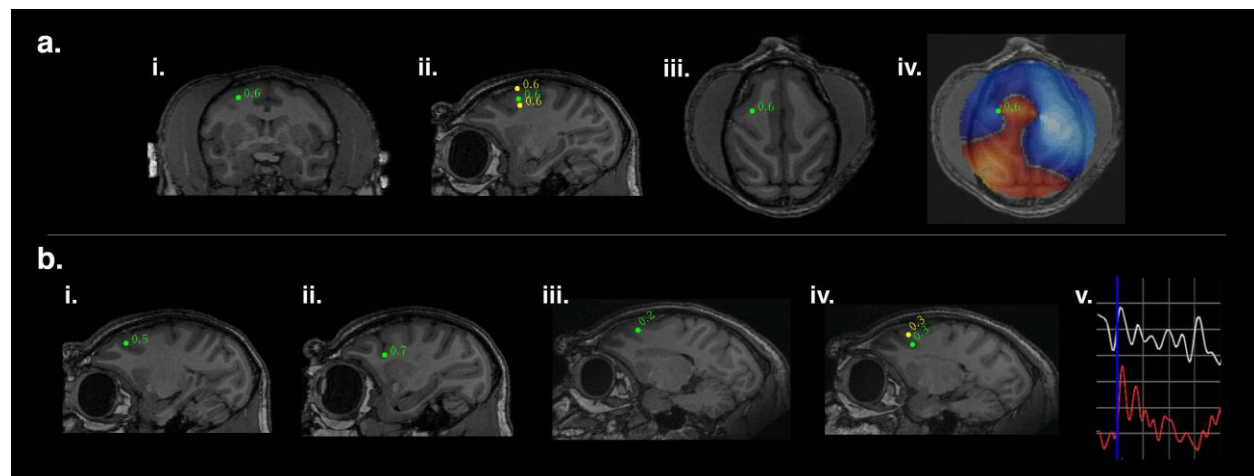
Figure 2. SAM source localization of optogenetically evoked MEG responses in the right arcuate sulcus. a. An example of optogenetic stimulation localized by dual-state SAM to the posterior bank of right arcuate sulcus in the coronal (**i**), sagittal (**ii**), and axial planes (**iii**), for a stimulus of 50 ms square light pulses. The whole brain, un-thresholded, dual-state SAM SPM (voxel size of 750 μm³, **iv**) reveals synchronized activity (red voxels) arising from the stimulation site and surrounded by desynchronization (blue voxels). Green dot and number indicate a peak in the SPM plus the associated pseudo-t value. **b.** Right SAM arcuate peaks for four additional and different optical stimuli in two different NHPs. **bi-ii** present arcuate activations for one NHP and **iii-iv** shows arcuate stimulation for a second NHP. **bi-ii** is the same subject as presented in **ai-iv**; **i** depicts the arcuate peak for 8 Hz sine waves, and **ii** shows the arcuate peak for 40 Hz sine waves. Arcuate stimulations in a second NHP are presented in **iii-iv**; **iii** shows the arcuate peak for 10 ms square pulses and **iv** shows the arcuate peak for 20 Hz square wave pulse trains. A single trial (**v**) of an LFP recorded by the optrode and a simultaneous SAM virtual electrode for an arcuate peak (as seen in **biii**). Blue vertical line indicates stimulus onset (10 ms pulses). Both the LFP (white) and virtual electrode (red) exhibit a rapid peak following stimulation and have similar features and time courses. One gray square in the graph = 100 ms on the abscissa and for the ordinate, 35 μV for the LFP or 15 nA-m for the virtual electrode. All maps follow radiological conventions.

663

664
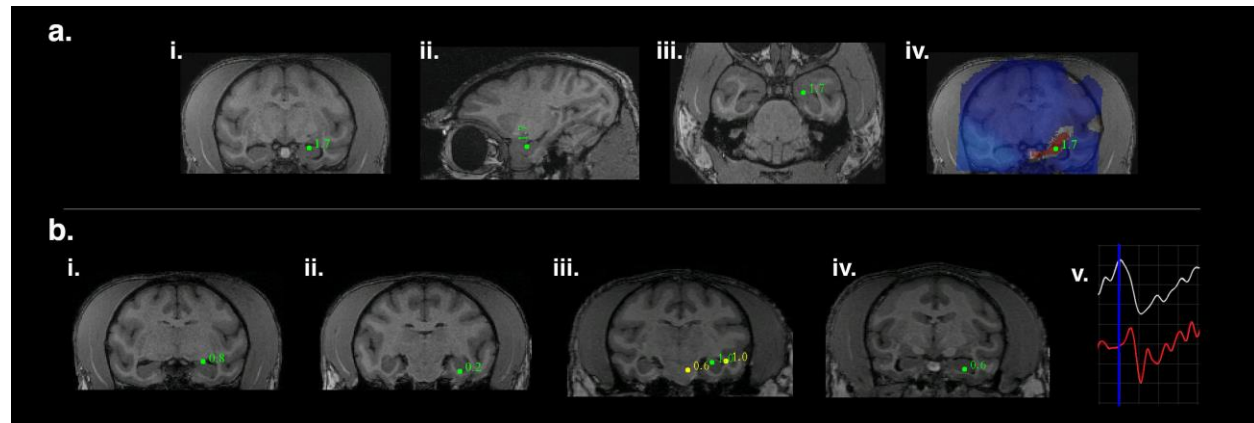
Figure 3. SAM source localization of optogenetically evoked MEG responses in the left hippocampus. a. SAM left hippocampal peak in coronal (**i**), sagittal (**ii**), and axial planes (**iii**) for a 20 Hz sine wave input in a third NHP. The whole brain, un-thresholded, SAM SPM shows synchronized activity arising from the stimulation site and surrounded by desynchronization (**iv**). **b.** Left SAM hippocampal peaks for four additional and different stimuli in two different NHPs. **bi-ii** is the same subject as presented in **a**; **i** and **ii** show hippocampal peaks for single 150 ms sawtooth trials or 10 ms square pulses, respectively. **biii-iv** show hippocampal peaks for 8 Hz or 40 Hz sine waves, respectively, in the same subject as in **Figure 2a**. A single trial (**v**) of a simultaneous LFP and SAM virtual electrode for hippocampus (as seen in **bi**). Blue vertical line indicates stimulus onset (sawtooth inputs). Both the LFP (white) and virtual electrode (red) peak rapidly following stimulation and have similar features and time courses. One gray square = 50 ms (abscissa) and 5 V for the LFP (amplified) or 500 nA-m for the virtual electrode (ordinate).

671

672

673

674

675

676

677

678

679

680

681

682

683
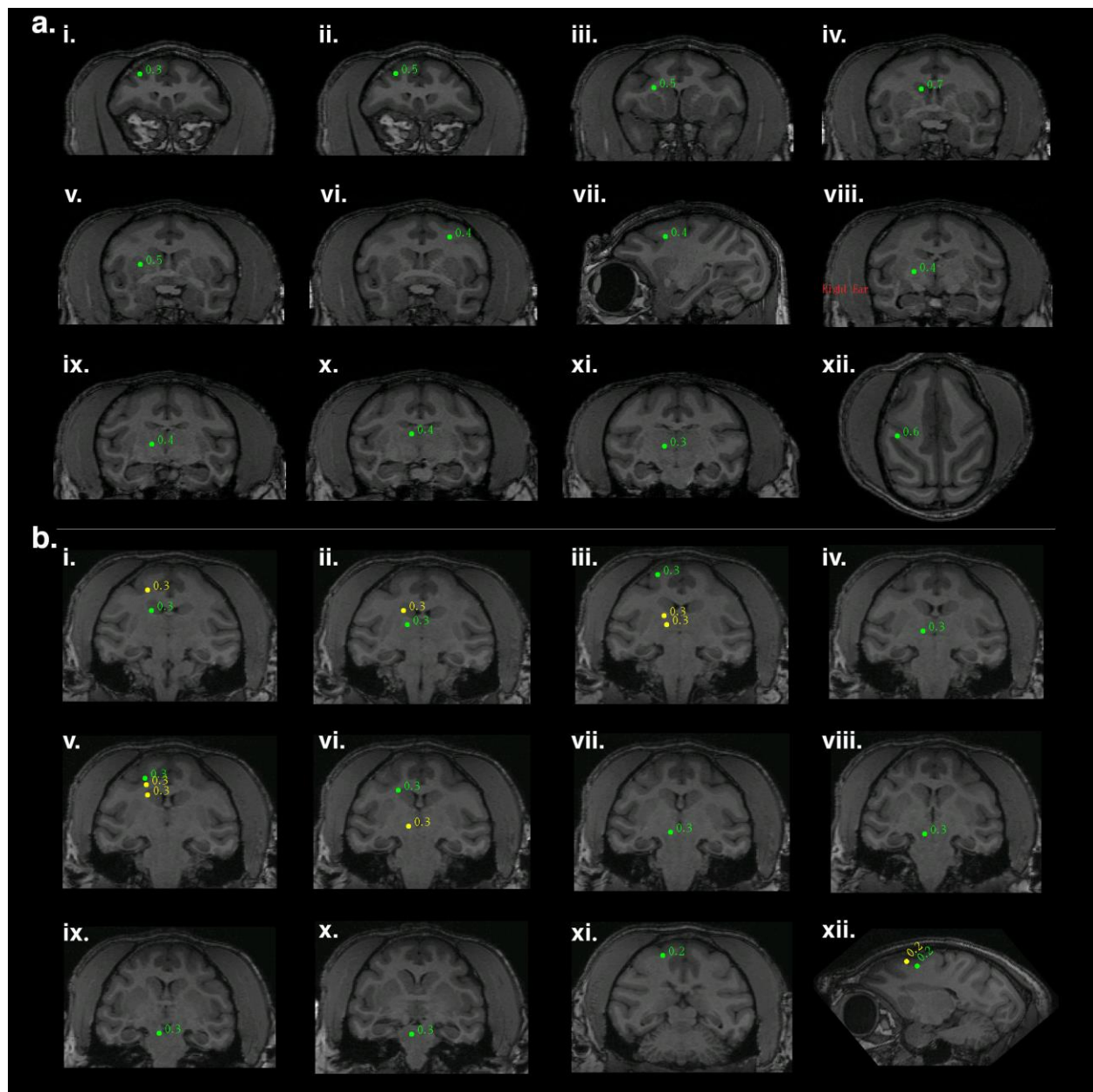
684 **Figure 4. Arcuate optogenetic stimulation results in propagation through downstream networks. a.** Identification of
685 cortico-striato-pallido-thalamo-cortical (CSPTC) network activity in response to 8 Hz sine wave stimulation of right
arcuate sulcus. SAM analysis of optical input to arcuate sulcus reveals a known functional network with peaks in: **i.** right
686 inferior bank arcuate sulcus, **ii.** right superior bank arcuate sulcus, the site of stimulation, **iii.** right corona radiata/
dorsolateral caudate n., **iv.** right caudate n. **v.** right putamen/ external segment of globus pallidus, **vi.** and **vii.** posterior
687 bank of contralateral (left) arcuate sulcus, coronal and sagittal slices, respectively, **viii.** right globus pallidus, **ix.** right
ventroposterior medial / ventroposterior lateral n. of thalamus, **x.** right medial dorsal n. of thalamus, **xi.** right ventral
688 posterior thalamus, and **xii.** parietal-occipital association area of the intraparietal sulcus. **b.** A second example of right
hemispheric CSPTC network activity in a different NHP in response to 20 Hz square wave pulse trains with SAM peaks as
689 follows: **i.** caudate n. (green) and cortical area 3 (yellow), **ii.** thalamus (green) and caudate n. (yellow), **iii.** posterior
dorsal bank of the arcuate sulcus (green) and two thalamic peaks (yellow), **iv.** thalamus, **v.** posterior ventral bank of
690 arcuate sulcus (green, site of stimulation), corpus callosum (yellow), and caudate n. (yellow), **vi.** caudate n. (green) and
mesencephalic nuclei (yellow), **vii.** mesencephalic n., **viii.** substantia nigra, **ix.** tegmental n., **x.** pontine or mesencephalic
n., and **xi.**, and **xii.** all peaks in primary motor cortex (area 4).
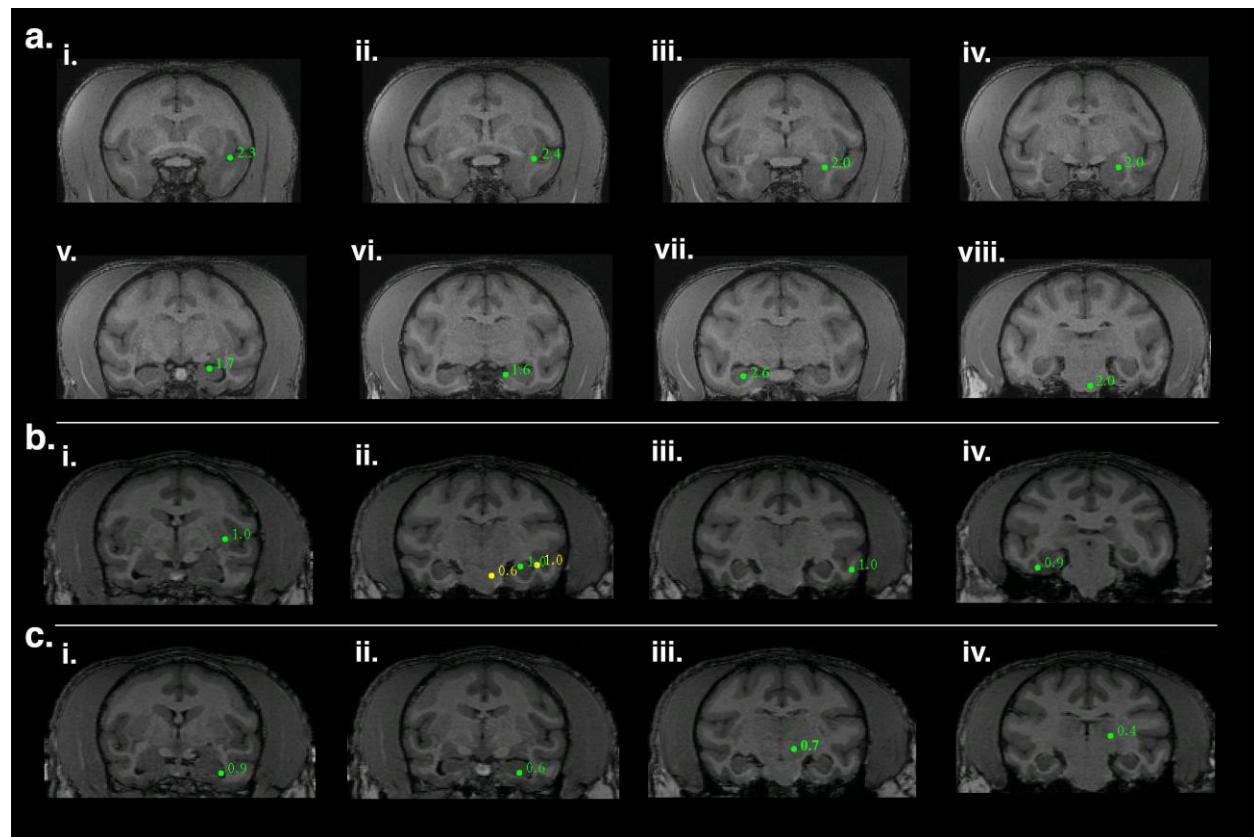
Figure 5. Hippocampal optogenetic stimulation results in propagation through downstream networks. a. Functional hippocampal and temporal network engaged by a 20 Hz optical sine input to left hippocampus (**v**) with SAM peaks as follows: **i.** left insular proisocortex/temporopolar proisocortex, **ii.** left para-insular cortex, **iii.** left dorsolateral amygdala (lateral n.), **iv.** left basolateral/lateral amygdala, **v.** left hippocampus, site of stimulation, **vi.** left parasubiculum/presubiculum of hippocampus, **vii.** contralateral (right) hippocampus, and **viii.** left pontine reticular activating formation. **b.** A second example of hippocampal network activity in a different NHP in response to 8 Hz sine wave input with SAM peaks as follows: **i.** left putamen, **ii.** PGa/IPa association areas of left temporal cortex (lateral yellow peak), left hippocampus (green peak, site of stimulation), and possible left red n. (yellow, medial peak), **iii.** area TEA/TEM of left temporal cortex, and **iv.** area TL/TFM of right temporal cortex. **c.** A third example of hippocampal network activity in response to 40 Hz sine wave input (same subject as in **b.**) with SAM peaks as follows: **i.** left anterior hippocampus, **ii.** left hippocampus, site of stimulation, **iii.** left deep mesencephalic n., and **iv.** left pulvinar n. of thalamus.

705

706

707

708
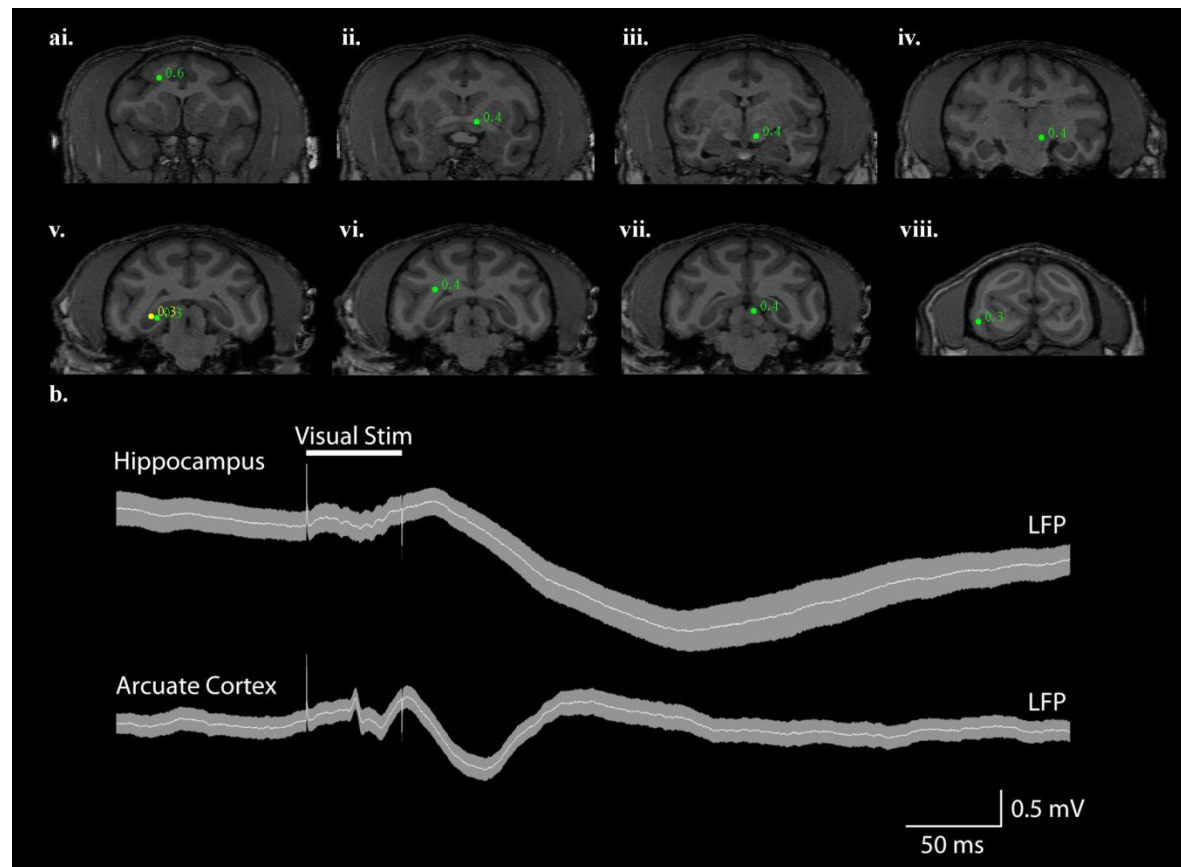
Supplementary Figure 1. Visual stimulation engages related brain regions. a. Identification of functional networks in response to 50 ms light presentations to the left lower visual quadrant of the left eye. SAM analysis of the visual stimulus reveals both peaks in the known visual network as well as additional peaks, including: **i.** right anterior arcuate sulcus, **ii.** left anterior commissure, **iii.** left optic tract, **iv.** left lateral geniculate n. **v.** right posterior hippocampus, **vi.** right posterior white matter tracts, **vii.** left superior colliculus, and **viii.** right occipital cortex. **b.** LFPs recorded from right arcuate cortex and left hippocampus revealed clear event-related potentials in response to visual stimulation.